Single-crystal study of the charge density wave metal $LuNiC_2$

S. Steiner, H. Michor,* O. Sologub, B. Hinterleitner, F. Höfenstock, M. Waas, and E. Bauer
Institute of Solid State Physics, TU Wien, A-1040 Wien, Austria

B. Stöger
X-Ray Center, TU Wien, Getreidemarkt 9, A-1060 Wien, Austria

V. Babizhetskyy, V. Levytskyy, and B. Kotur
Department of Inorganic Chemistry, Ivan Franko National University of Lviv, Kyryla and Mefodiya Str., 6, UA-79005 Lviv, Ukraine

(Received 7 February 2018; published 10 May 2018)

We report on single-crystal growth, single-crystal x-ray diffraction, physical properties, and density functional theory (DFT) electronic structure as well as Fermi surface calculations for two ternary carbides, $LuCoC_2$ and $LuNiC_2$. Electrical resistivity measurements reveal for $LuNiC_2$ a charge density wave (CDW) transition at $T_{CDW} \simeq 450$ K and, for $T > T_{CDW}$, a significant anisotropy of the electrical resistivity, which is lowest along the orthorhombic a axis. The analysis of x-ray superstructure reflections suggest a commensurate CDW state with a Peierls-type distortion of the Ni atom periodicity along the orthorhombic a axis. DFT calculations based on the CDW modulated monoclinic structure model of $LuNiC_2$ as compared to results of the orthorhombic parent type reveal the formation of a partial CDW gap at the Fermi level which reduces the electronic density of states from $N(E_F) = 1.03$ states/eV f.u. without CDW to $N(E_F) = 0.46$ states/eV f.u. in the CDW state. The corresponding bare DFT Sommerfeld value of the latter, $\gamma_{DFT}^{CDW} = 0.90$ mJ/mol K^2, reaches reasonable agreement with the experimental value $\gamma = 0.83(5)$ mJ/mol K^2 of $LuNiC_2$. $LuCoC_2$ displays a simple metallic behavior with neither CDW ordering nor superconductivity above 0.4 K. Its experimental Sommerfeld coefficient, $\gamma = 5.9(1)$ mJ/mol K^2, is in realistic correspondence with the calculated, bare Sommerfeld coefficient, $\gamma_{DFT} = 3.82$ mJ/mol K^2, of orthorhombic $LuCoC_2$.

DOI: 10.1103/PhysRevB.97.205115

I. INTRODUCTION

Intermetallic rare-earth nickel dicarbides, $RNiC_2$ (R = La, . . . ,Lu), with the noncentrosymmetric orthorhombic $CeNiC_2$ structure type [1,2], exhibit a variety of exciting physical phenomena. The initial interest focused (i) on their rare-earth magnetism (see, e.g., Refs. [3–5]) and, subsequently, (ii) on $LaNiC_2$, which exhibits superconductivity below about $T_c = 2.9$ K [6,7] with a time reversal symmetry broken order parameter [8,9], and (iii) on the multiple charge density wave (CDW) transitions of $PrNiC_2$, $NdNiC_2$, . . . ,$TmNiC_2$ [10–12] and, finally, (iv) on the complex interplay of magnetic and incommensurate as well as commensurate CDW order parameters [13–17] (see Ref. [18] for a review). The Peierls temperature, i.e., onset of CDW order, increases inversely proportional to the unit cell volume of $RNiC_2$ compounds [12] and is thus largest for $LuNiC_2$, which has not yet been studied in closer detail.

In the present work we investigate two lutetium 3d-metal dicarbides, $LuCoC_2$ and $LuNiC_2$ (initially reported by Jeitschko and Gerss [2]), with respect to their crystal structure, their electronic ground state properties, and in particular, with respect to the occurrence of charge density wave or superconducting transitions, by means of specific heat, magnetization, and electrical resistivity measurements as well as computational electronic structure and Fermi surface studies.

II. EXPERIMENTAL DETAILS

Polycrystalline samples, $LuCoC_2$ and $LuNiC_2$, have been prepared by arc melting with subsequent annealing at 1000 °C for 10 days using a preparation procedure described earlier [19]. Commercially available elements, Lu distilled bulk pieces (Metall Rare Earth; purity of 99.9 at. % and 99.99% Lu/R), powders of electrolytic nickel and cobalt (Strem Chemicals; 99.99 at. %), and graphite powder (Aldrich; 99.98 at. %) were used.

A first attempt to grow $LuCoC_2$ and $LuNiC_2$ single crystals has been conducted via the Czochralski method, by which we have earlier succeeded to grow $HoCoC_2$ [20]. In the present work on $LuNiC_2$, however, Czochralski pulling resulted in rather small single-crystalline domains (of the order of cubic-millimeter size) and just slightly larger crystalline domains in the case of $LuCoC_2$. The latter has been used for a specific heat measurement (see below).

A large single crystal of $LuNiC_2$ (> 200 mm^3) was finally grown from a stoichiometric polycrystalline feed rod via the floating zone technique in an optical mirror furnace (Crystal Systems Corporation, Japan) and was oriented by means of the Laue method. A cross section of the crystal (parallel and perpendicular to the growth direction) was examined with a

*michor@ifp.tuwien.ac.at

scanning electron microscope (SEM) using a Philips XL30 ESEM with EDAX XL-30 EDX detector. Thereby, a relatively homogeneous distribution of small inclusions (multiphase precipitates of typically 5–10 μm size, essentially composed from transparent Lu-C-O crystals and metallic Lu-Ta-C as well as Ni rich Lu-Ni-C phases) inside the single-crystalline matrix $LuNiC_2$ is resolved by SEM, but remains below the resolution limit of the powder x-ray diffraction (XRD) pattern (see below). From the density of precipitates in the SEM image, we roughly estimate a volume fraction of impurity phases of the order of 0.1% of the total crystal volume.

Powder XRD data of $LuCoC_2$ and $LuNiC_2$ were collected on a Siemens D5000 powder diffractometer with graphite monochromated Cu $K\alpha$ radiation ($20^\circ \leqslant 2\Theta \leqslant 120^\circ$, step size 0.02°). While powder XRD revealed the presence of some impurity phases in the polycrystalline material of $LuCoC_2$ and $LuNiC_2$, Bragg intensities due to impurity phases have neither been resolved in powder XRD for the Czochralski grown crystalline material of $LuCoC_2$ and $LuNiC_2$, nor for pieces of the zone refined $LuNiC_2$ crystal.

Crystals for XRD were isolated via mechanical fragmentation of the annealed $LuNiC_2$ and $LuCoC_2$ samples. Single-crystal x-ray intensity data were collected at $T = 100$ and 298 K on a four-circle Bruker APEX II diffractometer (CCD detector, κ geometry, Mo $K\alpha$ radiation, $\lambda = 0.710\,73$ Å). Multiscan absorption correction was applied using the program SADABS; frame data were reduced to intensity values applying the SAINT-PLUS package [21]. The structures were solved by direct methods and refined with the SHELX-97 and SHELXL-97 programs [22], respectively.

Zero-field specific heat data of single-crystalline samples of about 60 mg of $LuCoC_2$ and 100 mg of $LuNiC_2$ were collected in the temperature range 400 mK to 15 K using a physical property measurement system (PPMS) ^{3}He heat capacity insert.

Four-probe resistivity measurements were carried out on bar-shaped samples with contacts made by spot-welding thin gold wires ($d = 50$ μm) on the sample surface. For better mechanical stability, the spot-welded contacts were coated with silver epoxy. $LuNiC_2$ single-crystalline bar-shaped samples were cut along the principle crystallographic orientations with typical dimensions $0.7 \times 0.9 \times 5$ mm^3 and measured in a PPMS resistivity setup (2–400 K) as well as in a home-made furnace setup (300–610 K) with the identical set of samples. High-temperature resistivity measurements of polycrystalline samples $LuCoC_2$ and $LuNiC_2$ were performed in a ULVAC ZEM-3 measuring system (300–650 K). Temperature and field dependent magnetic measurements were carried out on a Cryogenic superconducting quantum interference device magnetometer in a temperature range from 2 K to room temperature applying static magnetic fields up to 7 T.

TABLE I. Unit cell parameters (structure type $CeNiC_2$, space group $Amm2$, No. 38, $Z = 2$), atomic coordinates, and anisotropic displacement parameters as well as experimental and refinement parameters; crystal structure data are standardized using the program STRUCTURE TIDY [32]. Diffraction data were collected at $T = 298$ K.

	$LuCoC_2$	$LuNiC_2$
a (Å)	3.4226(2)	3.4506(2)
b (Å)	4.4895(3)	4.4787(2)
c (Å)	5.9916(4)	5.9857(3)
Lu in $2b$ ($\frac{1}{2}$,0,z)	$z = 0.3835(1)$	$z = 0.3885(2)$
Occupation factor	1.00	1.00
U_{11}^{b}(Å^2)	0.0079(1)	0.0070(1)
U_{22}(Å^2)	0.0080(1)	0.0108(1)
U_{33}(Å^2)	0.0085(1)	0.0084(1)
M^a in $2a$ (0,0,0)		
Occupation factor	0.984 (6)	1.00
U_{11}^{b}(Å^2)	0.0098(4)	0.0217(5)
U_{22}(Å^2)	0.0060(3)	0.0060(3)
U_{33}(Å^2)	0.0070(4)	0.0068(4)
C in $4d$ (0,y,z)	$y = 0.3458(9)$	$y = 0.3444(11)$
	$z = 0.1890(7)$	$z = 0.1873(9)$
Occupation factor	1.00	1.00
U_{iso}(Å^2)	0.0088(6)	0.0097(7)
Theta range (deg.)	$5.68 < \theta < 37.05$	$5.69 < \theta < 34.87$
Crystal size (μm)	$48 \times 50 \times 55$	$55 \times 55 \times 60$
Reliability factors[c]	$R_F^2 = 0.0095$	$R_F^2 = 0.0119$
GOF	1.043	1.166
Extinction (Zachariasen)	0.0149(9)	0.0144(10)
Residual density: max; min (e^-/Å^3)	0.801; −0.742	0.847; −1.362

[a] M = Co or Ni.
[b] $U_{23} = U_{13} = U_{12} = 0$.
[c] $R_F^2 = \sum |F_0^2 - F_c^2| / \sum F_0^2$.

III. COMPUTATIONAL METHODS

Density functional theory (DFT) calculations based on the $CeNiC_2$-type orthorhombic structure models of $LuCoC_2$ as well as $LuNiC_2$ were performed within the projector augmented wave methodology [23] implemented in the Vienna *ab initio* simulation package (VASP) [24,25]. The generalized gradient approximation, as parametrized by Perdew, Burke, and Ernzerhof [26], was applied for the exchange potential. For the valence state configurations of the pseudopotentials we included the $5d^1 6p^6 6s^2$ states for Lu (the $4f$ electrons were kept frozen in the core), the $3p^6 3d^8 4s^1$ states for Co, the $3p^6 3d^9 4s^1$ states for Ni, and the $2s^2 p^2$ states for the C atoms. The remaining electrons were kept frozen.

The atom positions were relaxed with fixed experimental lattice constants (see Table I). During the relaxation, the total energy was minimized until the energy convergence became better than 1×10^{-8} eV. To obtain the equilibrium positions of the ions, residual forces were optimized until they undermatched 1×10^{-2} eV/Å. The Brillouin zone integration for the relaxation was done on a $10 \times 8 \times 6$ grid of **k** points on a Monkhorst and Pack [27] mesh using the method of Methfessel-Paxton [28] of the order one with a smearing parameter $\sigma = 0.1$, which results in well-converged total energies and optimized ionic positions. We note that complementary DFT calculations with a full relaxation of the $CeNiC_2$-type structure model (i.e., including the volume and lattice constants) closely reproduced all the below results obtained with a fixed cell shape.

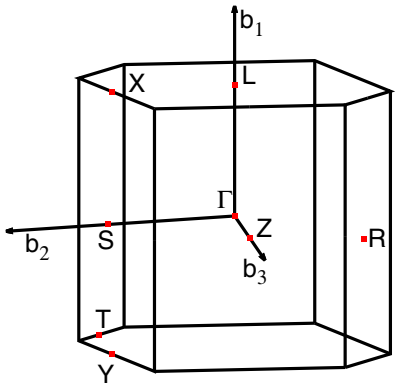

FIG. 1. The first Brillouin zone of the orthorhombic $CeNiC_2$-type structure including high-symmetry points (see text).

The electronic band structure (BS) was calculated using fully relaxed ionic positions with fixed cell shape and volume taking into account spin-orbit coupling (SOC) for the valence electrons as described in [29]. For the evaluation of the electronic density of states (EDOS) a dense $20 \times 16 \times 12$ **k**-point mesh has been implemented. The **k**-point integration was done using the tetrahedron method with Blöchl corrections [23]. The Brillouin zone integration for the BS was done using again the method of Methfessel-Paxton [28]. The electronic BS is plotted along high-symmetry **k** points in the irreducible Brillouin zone (IRBZ) as depicted in Fig. 1. These special **k** points in reciprocal space are $\Gamma = (0,0,0)$, $S = (0,\frac{1}{2},0)$, $R = (0,-\frac{1}{2},\frac{1}{2})$, $Z = (0,0,\frac{1}{2})$, $Y = (-\frac{1}{2},\frac{1}{2},0)$, $T = (-\frac{1}{2},\frac{1}{2},-\frac{1}{2})$, $X = (\frac{1}{2},\frac{1}{2},0)$, and $L = (\frac{1}{2},0,0)$; these **k** points are either a center of a face in IRBZ, a corner of IRBZ, or a midpoint of a line edge. We note that switching the space group setting from $Amm2$ to $Cm2m$, e.g., used in Refs. [7,30], leads to a commutation of axis (a,b,c) to (c,a,b) and thus to correspondent changes of the labeling of special **k** points in the IRBZ.

The Fermi surface is interpolated using maximally localized Wannier functions as implemented in the WANNIER90 code [31]. We have ascertained that the interpolated Wannier bands match well with the VASP bands in the region of interest, thus being suited to obtain reasonable Fermi surfaces.

For $LuNiC_2$, additional DFT calculations of the EDOS were performed for the CDW modulated structure model presented in Sec. IV A (see Table II) with a slightly adapted procedure: a variation of the volume and the cell shape was included in the relaxation procedure to overcome convergence problems, although the relative changes of the lattice constants during their relaxation did not exceed 3% and the relative deviation from the experimental volume remained within 2×10^{-3}. Relaxed atom coordinates are reasonably close to the experimental ones, e.g., yielding alternating Ni-Ni distances along the monoclinic b axis of 3.247 and 3.665 Å as compared to the experimentally refined values of 3.208(2) and 3.682(2) Å (see below). The optimization of residual forces was conducted with the same criteria, 1×10^{-2} eV/Å, as given above. For the Brillouin zone integration steps during relaxation, a grid of $5 \times 5 \times 9$ **k** points on a Monkhorst and Pack [27] mesh has been employed using the same method as for the $CeNiC_2$-type structure model.

TABLE II. Unit cell parameters and atomic coordinates as well as experimental and refinement parameters of the CDW superstructure of $LuNiC_2$ (space group Cm, No. 8) measured at $T = 100$ K.

	$LuNiC_2$
a (Å)	7.4662(9)
b (Å)	6.8897(9)
c (Å)	3.7326(5)
β (deg.)	106.324(3)
Lu1 in 2a $(x,\frac{1}{2},z)$	$x = -0.00866(6)$
	$z = -0.00807(8)$
Lu2 in 2a $(x,0,z)$	$x = 0.00866(5)$
	$z = 0.00807(8)$
Ni in 4b	$x = 0.1929(9)$
	$y = 0.2672(2)$
	$z = 0.6087(16)$
C1 in 4b	$x = 0.425(4)$
	$y = 0.2577(8)$
	$z = 0.448(6)$
C2 in 4b	$x = 0.268(4)$
	$y = 0.2501(7)$
	$z = 0.146(7)$
Theta range (deg.)	$4.13 < \theta < 49.68$
Crystal size (μm)	$80 \times 60 \times 20$
Reliability factors	$R_F^2 = 0.0294$
$(R_F^2 = \sum \lvert F_0^2 - F_c^2 \rvert / \sum F_0^2)$	
GOF	1.096
Extinction	0.0107(12)
(Zachariasen)	
Residual density:	3.097; −3.652
max; min ($e^-/\text{Å}^3$)	

The electronic DOS of the CDW modulated structure was calculated using the fully relaxed structure including SOC on a **k**-point mesh of $9 \times 10 \times 18$ with the tetrahedron method with Blöchl corrections [23] and $\sigma = 0.05$. The **k**-point mesh used for the CDW superstructure is lower than the mesh used for the $CeNiC_2$-type structure, because of its two times larger volume in real and, hence, correspondingly smaller Brillouin zone volume in the reciprocal space. Fermi surface calculations were performed with the same methods as for the parent-type structure model.

IV. RESULTS

A. Crystal structure determination from single-crystal XRD data

Single-crystal XRD data for $LuNiC_2$ and $LuCoC_2$ indicate a high degree of order (mosaicities <0.50). In contrast to $LuCoC_2$, $LuNiC_2$ features distinct superstructure reflections. Disregarding these reflections, the diffraction patterns of both $LuNiC_2$ and $LuCoC_2$ evidence orthorhombic symmetry with similar cell parameters. Systematic absences were consistent with the space groups $A222$, $A2mm$, $Am2m$, $Amm2$, and $Ammm$, out of which the noncentrosymmetric $Amm2$ proved to be correct during structure solution and refinement, as proposed earlier in Ref. [2]. Lu and transition-metal atom positions were deduced from direct methods with SHELXS-97 and refined in a straightforward manner using SHELXL-97; carbon

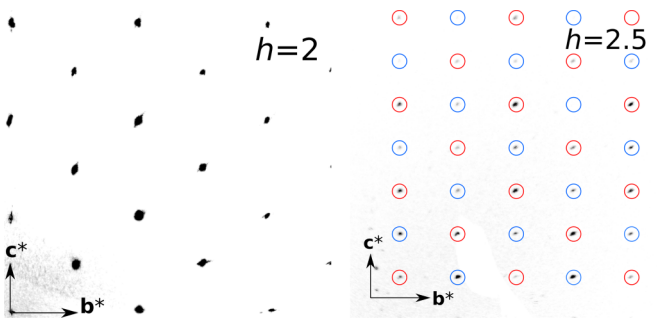

FIG. 2. $h = 2$ and $h = 2.5$ planes with respect to the reciprocal lattice of the $CeNiC_2$-type parent structure of $LuNiC_2$ reconstructed from CCD data in the left and the right panel, respectively. Superstructure reflections attributed to two different twin domains are marked by red and blue circles.

sites were easily located in the difference Fourier map. The refinements with free site occupation factors revealed some indication that the cobalt position in $LuCoC_2$ is occupied by about 98.4(6)%, whereas no deviations from full occupancies have been detected for the Lu and Ni atom positions. The final positional and atom displacement parameters obtained from single crystals are listed in Table I. A significant anisotropy of the atom displacement parameter with a substantially increased U_{11} ($U_{11} \simeq 3.6 \times U_{22} \simeq 3.2 \times U_{33}$) is observed only for Ni in $LuNiC_2$ which manifests some trace of CDW order in the refinement based on the orthorhombic $CeNiC_2$-type structure model.

To structurally characterize the CDW order, the superstructure reflections of a $LuNiC_2$ data set collected at 100 K and up to high diffraction angles ($2\theta = 100°$) were analyzed. Indexed in the reciprocal basis of the $Amm2$ parent structure, these superstructure reflections are located at $h = n_h + \frac{1}{2}, k = n_k + \frac{1}{2}, l = n_l + \frac{1}{2}, n_h, n_k, n_l \in \mathbb{Z}$ (Fig. 2). They can be attributed to two monoclinic C-centered (mC) domains, with the standard centered basis $[\mathbf{b} + \mathbf{c}, 2\mathbf{a}, (\mathbf{b} - \mathbf{c})/2]$ with respect to the parent structure. The monoclinic direction of the mC domains corresponds to the a axis of the orthorhombic parent structure. Assuming a symmetry reduction of the group/subgroup kind, only the Cm and Cc space groups are possible. Cc is ruled out owing to strong violations of the corresponding systematic absences. Indeed, only in the Cm space group were reasonable refinements obtained.

The lost orthorhombic symmetry is retained as twin law (twin operations $m_{[010]}, 2_{[001]}$ with respect to the orthorhombic basis). Whereas the main reflections of both domains overlap, the superstructure reflections form two disjoint sets (twinning by reticular pseudomerohedry; Fig. 2). A model of the CDW superstructure was constructed by symmetry reduction from the $Amm2$ model and refined against "HKLF5" data with information on reflection overlap. Crystal and refinement data as well as final coordinates are listed in Table II.

The symmetry reduction from the $Amm2$ parent to the Cm superstructure is of index four and can be decomposed into two steps, of the *translationengleiche* (reduction of point symmetry) and the *klassengleiche* (reduction of translation symmetry) type, respectively. The Lu position in the $CeNiC_2$-type parent structure with site symmetry $mm2$ is split into two positions with m site symmetry. The C position ($m..$) is split into two general positions. The site symmetry of the Ni atom is reduced from $mm2$ to 1, without being split. Consistent with the refinement of the parent structure (see above, Table I), the largest deviation from the $Amm2$ symmetry is observed for the Ni atoms. They are displaced distinctly along the monoclinic $b_{(s)}$ axis (being parallel to the orthorhombic a axis of the parent structure), thus forming pairs of Ni atoms related by the mirror reflection with a shortened Ni-Ni distance of 3.208(2) Å as compared to $b_{(s)}/2 = 3.445(1)$ Å. The large and highly anisotropic displacement parameters of Ni in the $Amm2$ averaged structure model become smaller and more isotropic in the Cm superstructure, i.e., comparing the anisotropic displacement matrix after main axis transformation, $U_{ii}/\text{Å}^2$ change from (0.0217,0.0068,0.0060) to (0.0077,0.0057,0.0042), respectively. The equidistant periodicity of the Ni atoms in the orthorhombic parent structure is thus replaced by alternating shortened and elongated Ni-Ni distances (3.208 vs 3.682 Å) which resemble a Peierls-type distortion, also referred to as a Peierls dimerization. The corresponding model of the CDW modulation of $LuNiC_2$ is depicted in Fig. 3 as views along the monoclinic $b_{(s)}$ axis in the upper and along the monoclinic $c_{(s)}$ axis in the lower panel. The latter emphasizes the Peierls-type distortion of the Ni atom periodicity along the $b_{(s)}$ axis, via fat blue solid lines highlighting the pairwise shortened Ni-Ni distances of 3.208(2) Å. The CDW modulation of the orthorhombic parent structure corresponds to a modulation wave vector $\mathbf{Q} = (\frac{1}{2}, 0, \frac{1}{2})$ in the IRBZ as displayed in Fig. 1.

B. Specific heat, magnetic susceptibility, and electrical resistivity of $LuCoC_2$ and $LuNiC_2$

The specific heat data displayed in Fig. 4 reveal for both $LuCoC_2$ and $LuNiC_2$ a metallic behavior, i.e., $C(T) \simeq \gamma T + (12\pi^4 n/5)(T/\Theta_D)^3$ at low temperatures, where γ represents the Sommerfeld coefficients of the T-linear electronic specific heat contribution, n is the number of atoms in the formula unit (i.e., $n = 4$ for $LuCoC_2$ and $LuNiC_2$), and Θ_D is the Debye temperature, characterizing the low-temperature lattice heat capacity. $LuCoC_2$ displays a distinct upturn in C/T at lowest temperatures (400–600 mK), which is similar to the one observed for elemental lutetium [33]. Such low-temperature upturn in C/T remains, at least for $T > 0.4$ K, absent for $LuNiC_2$. The corresponding linear fits of the data (see the dotted lines in Fig. 4) are applied to temperature intervals, $3 < T^2 < 60$ K^2 for $LuCoC_2$ and $T^2 < 40$ K^2 for $LuNiC_2$, thus yielding the Sommerfeld coefficients, $\gamma = 5.9(1)$ mJ/mol K^2 and 0.83(5) mJ/mol K^2 as well as Debye temperatures, $\Theta_D = 444$ (8) and 500 (10) K, respectively. While phonon specific heat contributions of $LuCoC_2$ and $LuNiC_2$ are closely matching each other in an extended temperature interval (not shown), electronic contributions of $LuCoC_2$ and $LuNiC_2$, and thus their electronic density of states at the Fermi level, $N(E_f)$, are strikingly different. For both $LuCoC_2$ and $LuNiC_2$, an anomaly, which could be indicative of bulk superconductivity, remains absent.

Field dependent magnetization and temperature dependent magnetic susceptibility measurements (not shown) reveal even for single-crystalline $LuNiC_2$, prepared by the floating zone technique, traces of a ferromagnetic impurity phase with

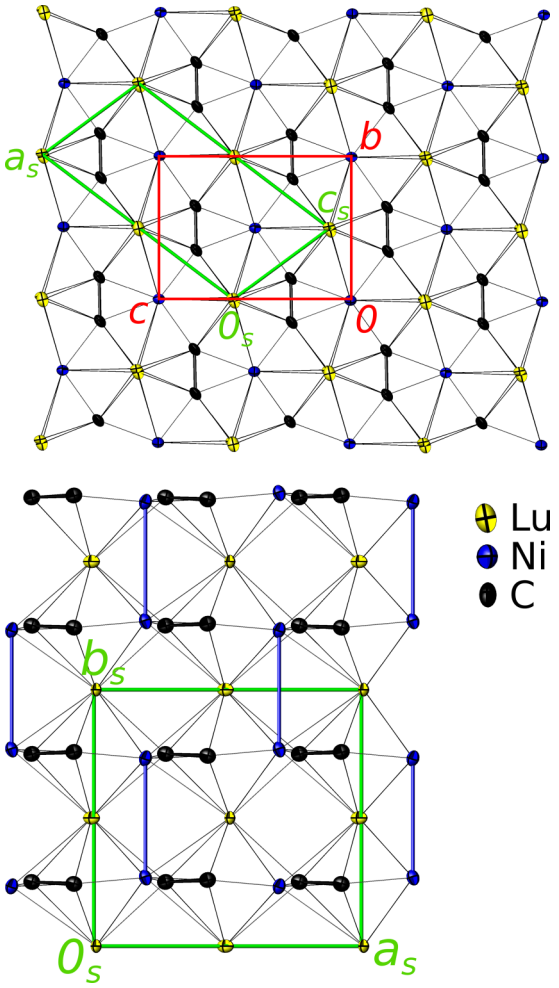

FIG. 3. Projection of the CDW superstructure as the view along the monoclinicic b axis ($||a$ axis of the orthorhombic cell) in the upper panel indicates the orthorhombic and monoclinic settings as red and green cells, respectively. The view along the monoclinicic c axis in the lower panel highlights the CDW superstructure modulation of the Ni-Ni distances.

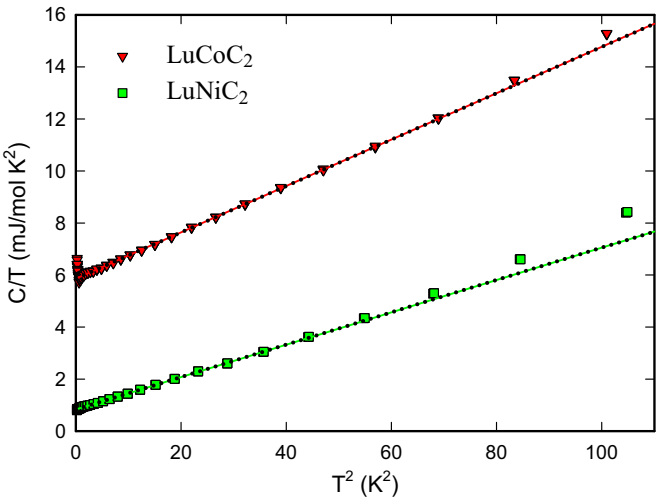

FIG. 4. Low-temperature specific heat as C/T vs T^2 of single crystals $LuCoC_2$ and $LuNiC_2$ as labeled; dotted lines are linear fits for limited temperature intervals (see text).

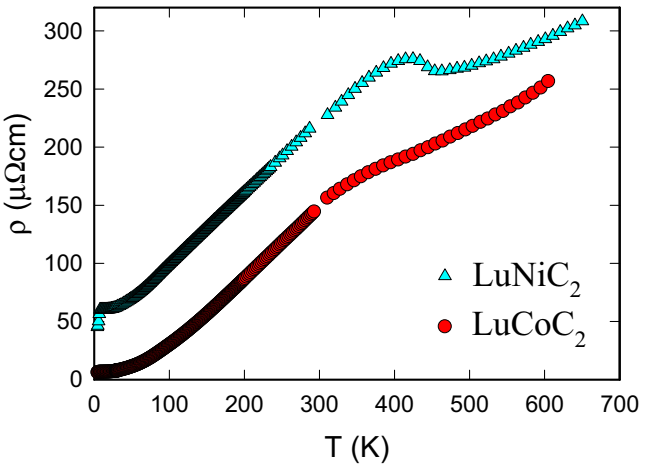

FIG. 5. Temperature dependent electrical resistivity, $\rho(T)$, of polycrystalline samples $LuCoC_2$ and $LuNiC_2$ as labeled.

$T_C \sim 80$ K ($\mu_{sat} \sim 2 \times 10^{-10} \mu_B$/f.u.) and of a superconducting impurity phase with $T_c \sim 5$ K. The isothermal magnetization, $M(H)$ measured at 2 K, is characteristic of a hard type-II superconductor with $H_{c1} \sim 5$ mT and $H_{c2} \sim 1$ T. The diamagnetic Meissner volume fraction is only about 5×10^{-3}, and thus attributed to a superconducting impurity phase precipitated in the zone refined crystal (compare SEM results in Sec. II). The intrinsic magnetic susceptibility of $LuNiC_2$ is diamagnetic with $\chi \simeq -2.2 \times 10^{-5}$ cm^3/mol at room temperature, which is roughly two-thirds of the expected core-diamagnetic susceptibility $\chi_{core} \sim -3 \times 10^{-5}$ cm^3/mol (see Ref. [34]). Both the ferromagnetic and the superconducting impurity phases are obviously well dispersed in the single-crystalline matrix in the form of small inclusions (see above).

Temperature dependent electrical resistivity measurements on polycrystalline samples displayed in Fig. 5 reveal a simple metallic behavior of $LuCoC_2$ with a reasonably low residual resistivity, $\rho_0 \simeq 7\ \mu\Omega$ cm, whereas for $LuNiC_2$ the residual resistivity, $\rho_0 \sim 50\ \mu\Omega$ cm, is largely enhanced and two distinct anomalies are observed at 7 K and near 450 K. The latter resembles the resistive CDW anomalies of other $RNiC_2$ compounds (with R = Pr–Tb), initially reported by Murase *et al.* [10], and is well in line with the trend of CDW transition temperatures, T_{CDW}, discussed in Ref. [12] where $T_{CDW} = 463$ K is suggested from preliminary results of $LuNiC_2$ which are in close agreement with the present data. The resistive drop observed at 7 K does not relate to any traceable, correspondent anomaly in the heat capacity, but does relate to a spurious diamagnetic signal of the magnetic susceptibility (see above) and is thus attributed to a small superconducting impurity fraction which is well below the percolation limit.

The anisotropy of the electrical resistivity of single-crystalline $LuNiC_2$, displayed in Fig. 6, is obtained from measurements with current applied along principal crystallographic orientations. The dotted vertical line in Fig. 6 marks the onset of CDW order at $T_{CDW} = 447$ (5) K. At temperatures exceeding the CDW transition, i.e., $T > T_{CDW}$, $LuNiC_2$ exhibits a similar anisotropy of the resistivity, $\rho_a < \rho_b < \rho_c$, as, e.g., reported earlier for $SmNiC_2$, $GdNiC_2$, and $TbNiC_2$ [11]. At

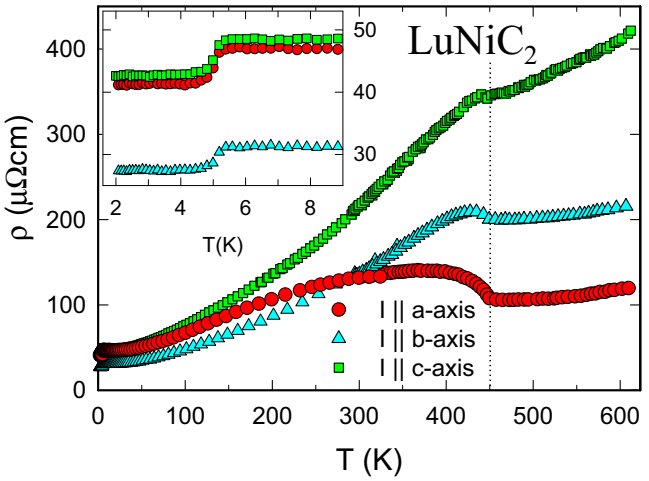

FIG. 6. Temperature dependent electrical resistivity, $\rho(T)$, of $LuNiC_2$ single crystals with the electric current applied parallel to crystal orientations as labeled. The dotted line indicates the onset of CDW order at 447(5) K.

lower temperatures ($T < T_{CDW}$), however, $LuNiC_2$ behaves distinctly different than the magnetic $RNiC_2$ single crystals investigated by Shimomura *et al.* [11]: (i) the CDW anomaly below T_{CDW} is most pronounced for ρ_a, while those of hitherto investigated magnetic $RNiC_2$ is most prominent for ρ_c and (ii) $LuNiC_2$ displays an almost isotropic electrical resistivity at $T < 50\,\mathrm{K}\,(\rho_a \sim 1.5\rho_b \sim \rho_c)$, whereas $\rho_a \ll \rho_b < \rho_c$ has been reported for magnetic $RNiC_2$. Finally, (iii) low-temperature resistive anomalies of the latter relate to the onset of rare-earth magnetism and the resulting modifications (suppression) of CDW order. $LuNiC_2$ displays a resistive anomaly near 5 K which is suppressed by an externally applied magnetic field (not shown). The critical field for suppressing the roughly isotropic resistivity drop by a few $\mu\Omega\,$cm is (independent of orientation) about 1 T at 2 K and decreases as a function of temperature as typical for a superconducting phase (see the above discussion of magnetization data).

C. Electronic structure studies of $LuCoC_2$ and $LuNiC_2$

1. Results based on the $CeNiC_2$*-type orthorhombic structure model*

Figure 7 displays the calculated electronic band structure of $LuCoC_2$ and $LuNiC_2$ for high-symmetry directions in the first Brillouin zone (compare Fig. 1). The dispersions are shown as a fat-band plot, which is a band structure equivalent to a projected EDOS plot. Thereby, symbols (brown circles for Lu site projected states, green triangles for C states, and red squares for the d-metal Co and Ni states) refer to the dominant atomic origin of the crystal orbitals and the widths of all bands are proportional to the relative contributions of a given set of atomic orbitals to the crystal orbitals. The upper panel of Fig. 7 reveals for $LuCoC_2$ that two Co 3d bands are crossing the Fermi energy. There is only some dispersion of these bands at Γ and R, else these bands are flat. Above the Fermi level, bands originate from mixed contributions from Co, C, and Lu and exhibit, in part, strong dispersion.

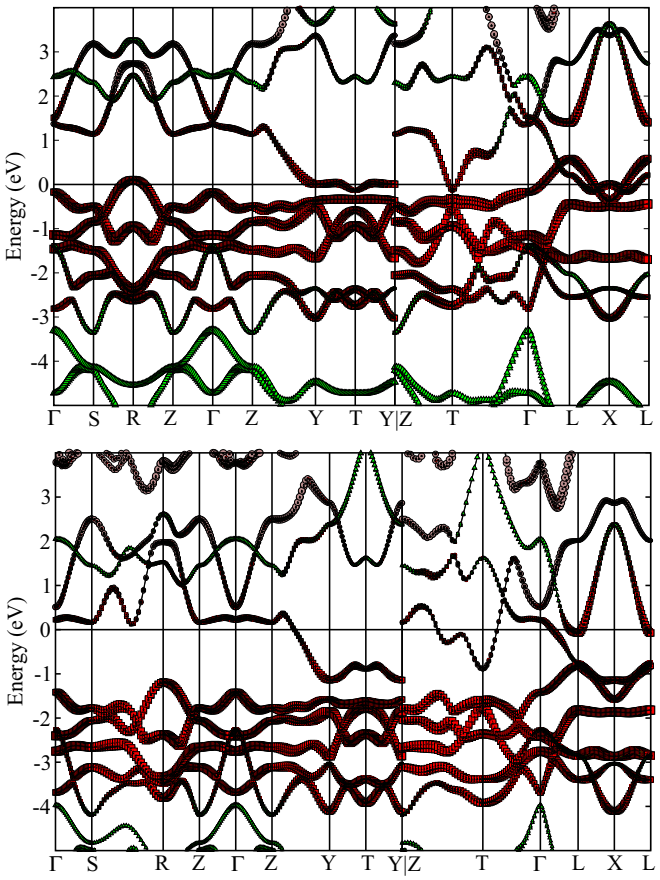

FIG. 7. Calculated electronic band structure of $LuCoC_2$ (upper panel) and $LuNiC_2$ (lower panel). In both plots brown circles denote a Lu character of the bands and green triangles denote a C related origin. In the upper panel, red squares refer to Co 3d dominated bands and in the lower panel to Ni 3d dominated bands. Zero energy (indicated by the horizontal line) refers to the position of the Fermi level. The diameter of the symbols shows the spectral weight related to each eigenstate of the system at a given k point.

For $LuNiC_2$ (lower panel of Fig. 7) a shift of the Fermi level by about 1 eV is observed (with respect to $LuCoC_2$), which almost resembles the expected filling of electronic states in terms of a rigid band picture. In the case of $LuNiC_2$, essentially one band with a mixed Lu-Ni-C character crosses the Fermi energy while the almost filled 3d dominated bands cross the Fermi level only near the L point located at the IRBZ boundary (compare Fig. 1) and originate a small electron pocket of the Fermi surface around this place (see below for further discussions of the Fermi surface).

In order to uncover the band splitting due to the asymmetric SOC caused by the lack of inversion symmetry of the crystal structure, Fig. 8 displays a closer view of the band structure in the vicinity of the Fermi level, where red and black lines refer to the two spin channels of SOC in the absence of inversion symmetry of the crystal structure. The largest splittings are observed for 3d dominated bands and, with respect to band crossing the Fermi level, spin-orbit splitting is most pronounced for $LuCoC_2$, while for $LuNiC_2$, smaller band splittings due to SOC are observed.

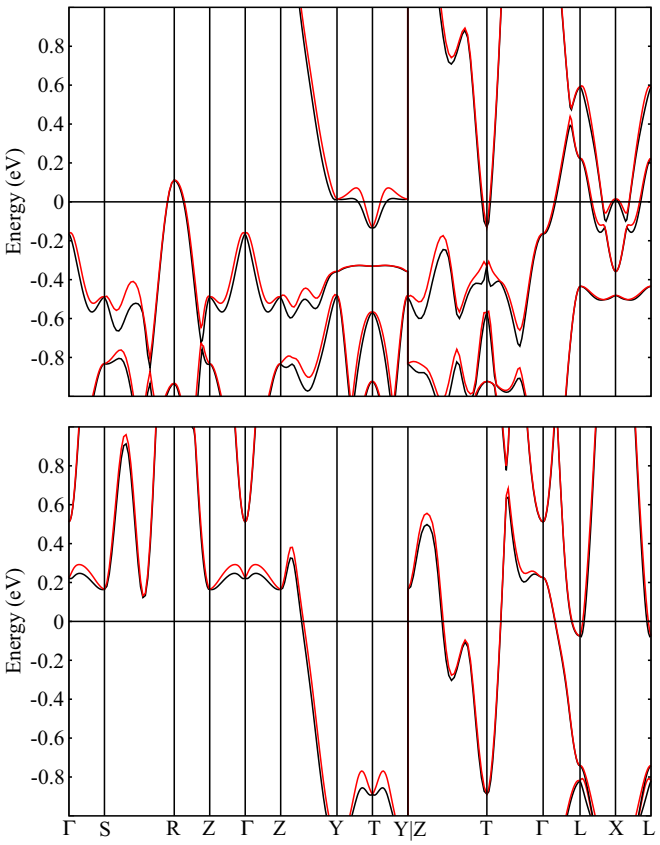

FIG. 8. Calculated electronic band structure of $LuCoC_2$ (upper panel) and $LuNiC_2$ (lower panel). Here a zoom of the BS is shown. The red and black curves refer to the two spin channels of SOC.

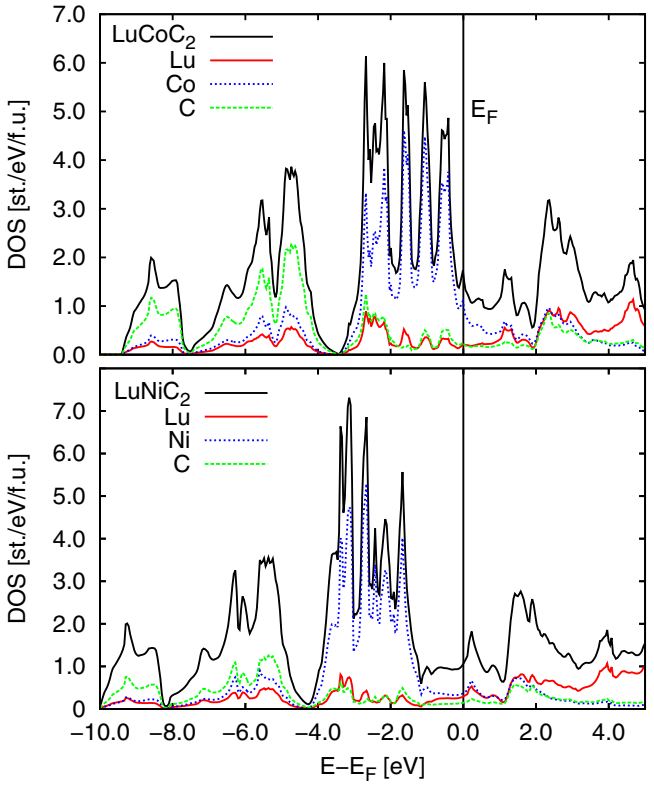

FIG. 9. Calculated electronic density of states for $LuCoC_2$ (upper panel) and $LuNiC_2$ (lower panel). The total EDOS is shown as a black solid line and the atom projected EDOS for Lu, Co and C sites are indicated as red solid, blue dotted, and green dashed lines, respectively.

Figure 9 presents the calculated EDOS of $LuCoC_2$ and $LuNiC_2$ in the upper and lower panel, respectively. Both EDOS plots have very similar features, except for the position of the Fermi energy, which relates to the different $3d$ electron count of Co as compared to Ni. The EDOS at the Fermi energy, $N(E_F)$, of $LuCoC_2$ and $LuNiC_2$ are 1.62 states/eV f.u. and 1.03 states/eV f.u., respectively. The corresponding site projected EDOS contributions at the Fermi level are dominated by about 80% by Co $3d$ contributions of $LuCoC_2$, whereas for $LuNiC_2$, there are almost equal contributions to $N(E_F)$ from Ni and Lu and still relevant ones from carbon projected states.

The Fermi surface of $LuNiC_2$, depicted in Fig. 10, consists of two sheets which are each moderately split by SOC into sheets related to the two spin channels of SOC. One is a pair of large quasiplanar sheets, which are connected by two neckings at the IRBZ boundary along the b_1 direction and the second is a small electron pocket centered at the L point of the IRBZ (compare Fig. 1). The larger Fermi surface sheet approximates to that of a quasi-one-dimensional electronic band and, with evolving modifications within the series $LaNiC_2$ to $LuNiC_2$, seems typical for $RNiC_2$ compounds. Calculations for early rare-earth members, $LaNiC_2$ and $SmNiC_2$, by Laverock *et al.* [35] suggested a similar pair of large sheets oriented perpendicular to the b_1 direction which, however, display an additional necking at the position of the electron pocket of $LuNiC_2$. Contrary to $LuNiC_2$, $LaNiC_2$ is reported in Ref. [35] to display a significant electron pocket centered at the Γ point, which becomes small for $SmNiC_2$ and is absent in the present calculation of $LuNiC_2$ and also in the Fermi surface calculation of $YNiC_2$ reported by Hase and Yanagisawa [30]. The latter results are in rather close match with the present ones of $LuNiC_2$ presented in Fig. 10.

Calculations of $LuCoC_2$ reveal the two Fermi surface sheets depicted in Fig. 11, where that of band 17 in the right panel corresponds to the large quasiplanar Fermi surface sheets of $LuNiC_2$, however, at a much lower band-filling state resulting

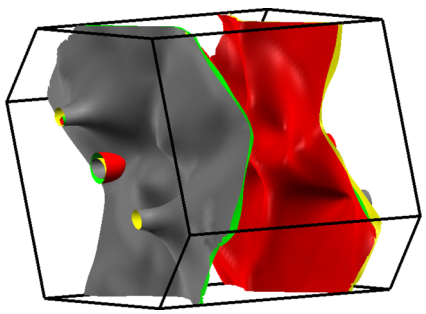

FIG. 10. The Fermi surfaces of $LuNiC_2$ displayed with orientation b_1 horizontally and b_2 vertically, as indicated by the first Brillouin zone boundaries. The two spin channels of SOC are indicated by colored sheets where red/yellow sides are toward unoccupied and green/gray sides are toward occupied states.

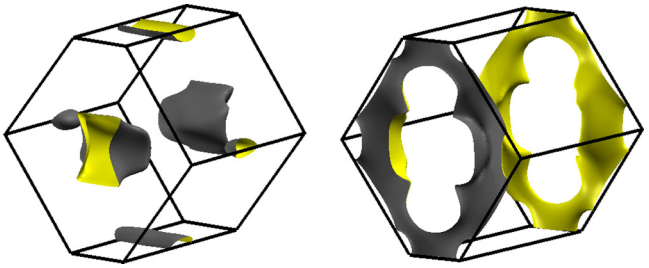

FIG. 11. Fermi surfaces of $LuCoC_2$ are depicted separately for two bands (neglecting SOC; see text): in the left panel, band 16 is displayed, and in the right panel, band 17. Gray and yellow sides face occupied and unoccupied states, respectively.

from the lower d-electron count of Co as compared to Ni. For the sake of clarity and focus on the essential features of the Fermi surface, the spin splitting due to the asymmetric SOC is neglected in Fig. 11.

2. *Comparison of* $LuNiC_2$ *results based on structure models with and without CDW modulation*

Figure 12 presents a direct comparison of the EDOS calculated for two structure models of $LuNiC_2$, the $CeNiC_2$-type parent structure and the CDW modulated structure, which reveals the formation of a partial CDW gap right at the Fermi energy. The value of the EDOS at the Fermi energy, $N(E_F) = 0.38$ states/eV f.u., of the CDW modulated structure is thus significantly reduced as compared to $N(E_F) = 1.03$ states/eV f.u. obtained for the orthorhombic parent structure of $LuNiC_2$.

The formation of a partial CDW gap is caused by the new Brillouin zone boundaries related to the CDW structure modulation which doubles the real-space unit cell volume. The Brillouin zone boundaries of the CDW superstructure intersect with the pair of large Fermi surface sheets of parent-type structure of $LuNiC_2$ which forms an extended two-dimensional structure oriented perpendicular to the b_1 direction in the orthorhombic periodic zone scheme displayed in the upper panel

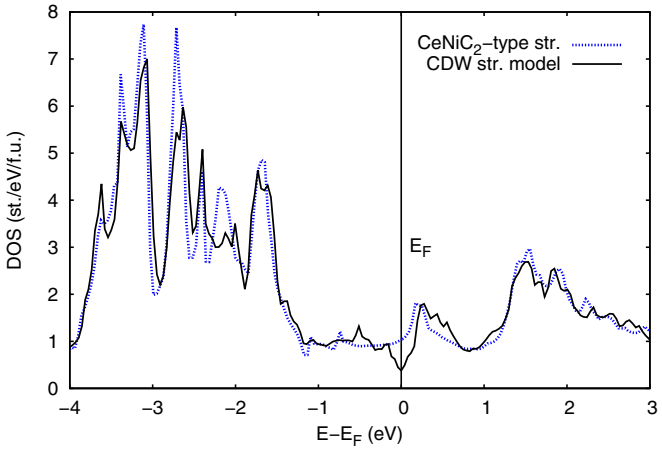

FIG. 12. Calculated electronic density of states of $LuNiC_2$ based on its structure models with and without CDW superstructure is shown as a black solid line and blue dotted line, respectively.

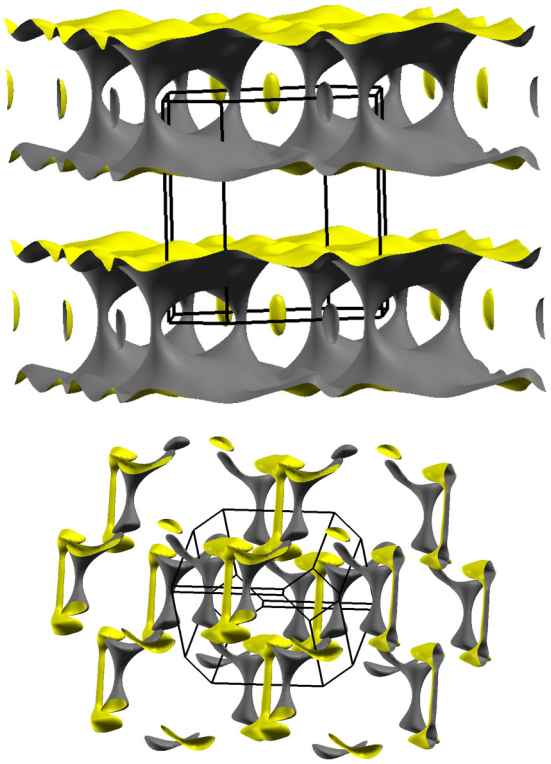

FIG. 13. Fermi surfaces of $LuNiC_2$ are displayed in a periodic zone scheme, for the sake of clarity without SOC, for the parent-type and the CDW modulated structure in the upper and lower panel, respectively. Gray and yellow sides face occupied and unoccupied states, respectively.

of Fig. 13. These quasiplanar (extended) Fermi surface sheets in the reciprocal space, manifest a quasi-one-dimensional electronic feature in real space. Our results of Fermi surface calculations of the CDW modulated structure displayed in a periodic zone scheme in the lower panel of Fig. 13 reveal a complete fragmentation of the extended Fermi surface of the orthorhombic parent structure into several isolated electron and hole pockets as the obvious consequence of introducing additional CDW superzone boundaries in the context of a CDW gap formation.

V. DISCUSSION

The comparison of the electronic Sommerfeld coefficient obtained from the experimental specific heat data of $LuNiC_2$, $\gamma = 0.83(5)$ mJ/mol K^2 (see Sec. IV B), with the bare Sommerfeld values, $\gamma_{DFT}^{CDW} \equiv N(E_F)k_B^2\pi^2/3 = 0.90$ mJ/mol K^2 for the CDW modulated structure and $\gamma_{DFT} = 2.43$ mJ/mol K^2 for the parent structure without CDW, reveals reasonably close agreement for the CDW model, but a rather large discrepancy for the DFT result of the orthorhombic parent structure of $LuNiC_2$. The latter is expected to be adopted at temperatures above $T_{CDW} \simeq 450$ K, at which electrical resistivity data indicate the partial CDW gap to vanish. On the other hand, there is a realistic agreement between the experimental Sommerfeld value of $LuCoC_2$, $\gamma = 5.9(1)$ mJ/mol K^2, and its corresponding calculated, bare electronic Sommerfeld value, $\gamma_{DFT} = 3.82$ mJ/mol K^2 of the $CeNiC_2$-type orthorhombic

structure model of $LuCoC_2$. The approximate enhancement of the experimental value by a factor of 1.5 as compared to the calculated one relates to a weak to moderate electron-phonon effective mass enhancement, $\gamma = \gamma_e(1 + \lambda_{ep})$, where $\lambda_{ep} \sim 0.5$ is the so-called electron-phonon mass enhancement factor.

The quasi-one-dimensional metallic nature of $LuNiC_2$ at $T > T_{CDW}$, which is indicated by the Fermi surface topology displayed in the upper panel of Fig. 13, is well corroborated by the significant anisotropy of the electrical resistivity at high temperatures, which, indeed, is lowest along the orthorhombic a axis, i.e., perpendicular to the orientation of the quasi-planar Fermi surface sheets. Within the CDW ordered state, i.e., below $T_{CDW} \simeq 450$ K, the partial CDW gap formation fragments these extended Fermi surface sheets into isolated Fermi surface pockets (compare Fig. 13) and thus conforms with the experimentally observed, more isotropic low-temperature electrical resistivity as compared to the high-temperature state without CDW order.

Some distinct differences between the observations from single-crystal resistivity studies of $LuNiC_2$ in Sec. IV B and correspondent results obtained for several magnetic $RNiC_2$ compounds investigated by Shimomura *et al.* [11] may relate to changes of the CDW modulations within the series of $RNiC_2$ compounds (compare Ref. [12]).

In order to discuss features of the Fermi surface of $LuNiC_2$ depicted in Fig. 10 in closer detail, we present in Fig. 14 slices of the Fermi surface as contour plots, where in the upper panel, for the sake of clarity, SOC is neglected. The z values therein refer to a parallel shift of these slices in units of the reciprocal lattice periodicity. Slices with identical orientation and position (except for $z = 0$) as those shown in the upper panel of Fig. 14, have earlier been presented by Laverock *et al.* [35] for $LaNiC_2$ and $SmNiC_2$ (the basis vector setting with $b^\star$ in Ref. [35] corresponds to $b_2 + b_3$ in the present work, while $a^\star = b_1$). A direct comparison of the Fermi surface contours of $LaNiC_2$ and $SmNiC_2$ in Ref. [35] with those of $LuNiC_2$ in Fig. 14 shows that the latter is getting closer to the idealized Fermi surface of a half-filled quasi-one-dimensional band with two (ideally planar) parallel sheets. Overall, the Fermi surface of the CDW metal $SmNiC_2$ ($T_{CDW} \simeq 148$ K [10]) reported by Laverock *et al.* [35] appears significantly more corrugated and slightly more deviant from half-filling than that of $LuNiC_2$.

An important aspect is revealed from the slice of IRBZ which exactly hosts the experimentally observed wave vector $\mathbf{Q} = (\frac{1}{2},0,\frac{1}{2})$ of CDW ordering, namely, the slice span by reciprocal lattice vectors b_1 and b_3 displayed in the lower panel of Fig. 14. The commensurate wave vector $\mathbf{Q} = (\frac{1}{2},0,\frac{1}{2})$ is shown as a black arrow and appears to roughly conform with a Fermi surface nesting vector which connects two quasiparallel parts of the Fermi surface contour, however, with a significant length mismatch of about 10%. Moreover, various other nesting features of similar or even higher significance can be found for q_n vectors which are clearly different from the structure modulation $\mathbf{Q}$. From the present results of Fermi surface calculations of $LuNiC_2$ in its orthorhombic parent-type structure we cannot confirm an obvious and dominant Fermi surface nesting at wave vector $\mathbf{Q} = (\frac{1}{2},0,\frac{1}{2})$. In the case of $SmNiC_2$, Laverock *et al.* [35] has indicated an even better match of the experimental structure modulation wave vector with a more extended Fermi surface nesting feature, although

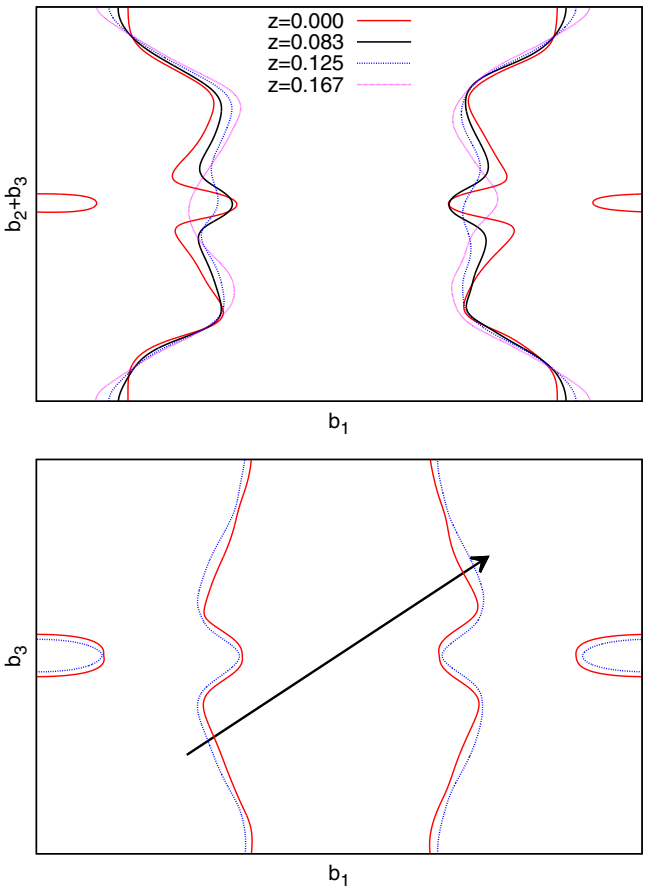

FIG. 14. Fermi surface contours of $LuNiC_2$ in parallel planes with offset z away from the plane intersecting the Γ point as labeled for planes spanned by reciprocal vectors b_1 and $b_2 + b_3$ are displayed, for the sake of clarity without SOC, in the upper panel. The lower panel shows Fermi surface contours calculated with SOC in the plane span by b_1 and b_3 at $z = 0$ (i.e., including the Γ point) and the CDW structure modulation vector $\mathbf{Q} = (\frac{1}{2},0,\frac{1}{2})$ is shown as a black arrow. The two spin channels of SOC are indicated in the lower panel by red solid and blue dashed lines.

the CDW ordering temperature is only one third as compared to $LuNiC_2$.

The absence of a clear correlation between the CDW ordering temperature and the degree of a Fermi surface nesting, which matches the structure modulation wave vector, in the series of $RNiC_2$ compounds seems in line with recent theoretical proposals by Johannes and Mazin [36] and by Gor'kov [37] suggesting that in real systems studied so far, CDW formation is driven by q-dependent electron-phonon coupling rather than by a simple electronic Fermi surface nesting mechanism. Deeper experimental and theoretical investigations of $LuNiC_2$, e.g., as compared to $YNiC_2$, may be suited to clarify the key factors which govern CDW ordering temperature in this system.

VI. SUMMARY AND CONCLUSIONS

$LuCoC_2$ and $LuNiC_2$ have been prepared in single-crystalline form. X-ray single-crystal diffraction confirmed $LuCoC_2$ to crystallize in the noncentrosymmetric

orthorhombic space group $Amm2$ and, apart from weak extra reflections related to twinned superstructure modulations, also the room temperature single-crystal XRD data of $LuNiC_2$ are rather well accounted for by this $CeNiC_2$-type structure model, however, with a significantly enhanced anisotropic displacement parameter U_{11} of the Ni site. From the analyis of $LuNiC_2$ crystal data taken at 100 K we derived a model of a monoclinic superstructure (space group Cm) which suggests a commensurate CDW modulation of the orthorhombic parent structure. The largest deviation from $Amm2$ symmetry of the $CeNiC_2$-type structure model is observed for the Ni atoms which are displaced along the orthorhombic a axis in the form of a Peierls-type distortion of the Ni atom periodicity with pairwise shortened Ni-Ni distances of 3.208(2) Å alternating with pairwise elongated distances of 3.682(2) Å.

Electrical resistivity and specific heat measurements of $LuCoC_2$ indicate a simple metallic behavior with neither CDW ordering nor superconductivity above 0.4 K. Analogous electrical resistivity studies of poly- as well as single-crystalline samples of $LuNiC_2$, however, reveal a metallic state with a CDW transition at $T_{CDW} \simeq 450$ K and a significant anisotropy of the electrical resistivity for $T > T_{CDW}$. The high-temperature resistivity is lowest along the orthorhombic a axis and highest along the c axis. CDW ordering causes a reduction of anisotropy of the electrical resistivity at lower temperatures.

The low-temperature specific heat results reveal significantly different electronic Sommerfeld coefficients, $\gamma = 5.9(1)$ mJ/mol K^2 for $LuCoC_2$ and $\gamma = 0.83(5)$ mJ/mol K^2 for $LuNiC_2$, while DFT calculations of the state before CDW ordering suggests much closer values of the electronic density of states at the Fermi level, $N(E_F) = 1.62$ states/eV f.u. for $LuCoC_2$ and $N(E_F) = 1.03$ states/eV f.u. for $LuNiC_2$. The large reduction of the experimental Sommerfeld coefficient of $LuNiC_2$ as compared to the calculated, bare band structure value, $\gamma_{DFT} = 2.43$ mJ/mol K^2, suggests that the Fermi surface of $LuNiC_2$ is strongly modified by CDW gap formation. DFT calculations based on the monoclinic CDW superstructure model, indeed, indicate the formation of a pronounced minimum right at the Fermi level and the corresponding DFT result of the Sommerfeld coefficient of the CDW modulated state, $\gamma_{DFT}^{CDW} = 0.90$ mJ/mol K^2, reaches close agreement with the experimental value.

The fact that $LuNiC_2$ displays the highest CDW ordering temperature among isostructural $RNiC_2$ compounds, even though a coincidence of the wave vector of the CDW modulation, $\mathbf{Q} = (\frac{1}{2}, 0, \frac{1}{2})$, with a predominant Fermi surface nesting vector remains weak, suggests a relevance of other mechanisms such as CDW formation due to strongly q-dependent electron-phonon coupling proposed in Refs. [36,37].

ACKNOWLEDGMENTS

Metallographic support by S. Stojanovic is gratefully acknowledged. We thank M. Abd-Elmeguid for fruitful discussions. The computational results have been achieved in part by using the Vienna Scientific Cluster (VSC) within Project No. 71074. The support of the VSC staff is gratefully acknowledged.

[1] O. I. Bodak, E. P. Marusin, and V. A. Bruskov, Kristallografiya **25**, 355 (1980) [Sov. Phys. Crystallogr. **25**, 617 (1980)].
[2] W. Jeitschko and M. Gerss, J. Less-Common Met. **116**, 147 (1986).
[3] P. Kotsanidis, J. Yakinthos, and E. Gamari-Seale, J. Less-Common Met. **152**, 287 (1989).
[4] W. Schäfer, W. Kockelmann, G. Will, J. K. Yakinthos, and P. A. Kotsanidis, J. Alloys Compd. **250**, 565 (1997).
[5] H. Onodera, Y. Koshikawa, K. Masashi, M. Ohashi, H. Yamauchi, and Y. Yamaguchi, J. Magn. Magn. Mater. **182**, 161 (1998).
[6] W. H. Lee, H. K. Zeng, Y. D. Yao, and Y. Y. Chen, Physica C (Amsterdam) **266**, 138 (1996).
[7] Y. Hirose, T. Kishino, J. Sakaguchi, Y. Miura, F. Honda, T. Takeuchi, E. Yamamoto, Y. Haga, H. Harima, R. Settai, and Y. Onuki, J. Phys. Soc. Jpn. **81**, 113703 (2012).
[8] A. D. Hillier, J. Quintanilla, and R. Cywinski, Phys. Rev. Lett. **102**, 117007 (2009).
[9] T. Yanagisawa and I. Hase, J. Phys. Soc. Jpn. **81**, SB039 (2012).
[10] M. Murase, A. Tobo, H. Onodera, Y. Hirano, T. Hosaka, S. Shimomura, and N. Wakabayashi, J. Phys. Soc. Jpn. **73**, 2790 (2004).
[11] S. Shimomura, C. Hayashi, N. Hanasaki, K. Ohnuma, Y. Kobayashi, H. Nakao, M. Mizumaki, and H. Onodera, Phys. Rev. B **93**, 165108 (2016).
[12] M. Roman, J. Strychalska-Nowak, T. Klimczuk, and K. K. Kolincio, Phys. Rev. B **97**, 041103 (2018).
[13] J. H. Kim, J.-S. Rhyee, and Y. S. Kwon, Phys. Rev. B **86**, 235101 (2012).
[14] G. Prathiba, I. Kim, S. Shin, J. Strychalska, T. Klimczuk, and T. Park, Sci. Rep. **6**, 26530 (2016).
[15] K. K. Kolincio, K. Górnicka, M. J. Winiarski, J. Strychalska-Nowak, and T. Klimczuk, Phys. Rev. B **94**, 195149 (2016).
[16] H. Lei, K. Wang, and C. Petrovic, J. Phys.: Condens. Matter **29**, 075602 (2017).
[17] K. K. Kolincio, M. Roman, M. J. Winiarski, J. Strychalska-Nowak, and T. Klimczuk, Phys. Rev. B **95**, 235156 (2017).
[18] V. Babizhetskyy, B. Kotur, V. Levytskyy, and H. Michor, in *Handbook on the Physics and Chemistry of Rare Rarths*, edited by J. C. Bünzli and V. K. Pecharsky (Elsevier, New York, 2017), Vol. 52, Chap. 298, pp. 1–263.
[19] H. Michor, V. Levytskyy, F. Schwarzböck, V. Babizhetskyy, and B. Kotur, J. Magn. Magn. Mater. **374**, 553 (2015).
[20] H. Michor, S. Steiner, A. Schumer, M. Hembara, V. Levytskyy, V. Babizhetskyy, and B. Kotur, J. Magn. Magn. Mater. **441**, 69 (2017).
[21] Bruker, APEXII, RLATT, SAINT, SADABS and TWINABS, Bruker AXS, Inc., Madison, WI, 2014.
[22] G. Sheldrick, Acta Crystallogr. **A64**, 112 (2008).
[23] P. E. Blöchl, Phys. Rev. B **50**, 17953 (1994).
[24] G. Kresse and J. Furthmüller, Phys. Rev. B **54**, 11169 (1996).
[25] G. Kresse and D. Joubert, Phys. Rev. B **59**, 1758 (1999).
[26] J. P. Perdew, K. Burke, and M. Ernzerhof, Phys. Rev. Lett. **77**, 3865 (1996).

[27] H. J. Monkhorst and J. D. Pack, Phys. Rev. B **13**, 5188 (1976).
[28] M. Methfessel and A. T. Paxton, Phys. Rev. B **40**, 3616 (1989).
[29] S. Steiner, S. Khmelevskyi, M. Marsmann, and G. Kresse, Phys. Rev. B **93**, 224425 (2016).
[30] I. Hase and T. Yanagisawa, J. Phys. Soc. Jpn. **78**, 084724 (2009).
[31] A. A. Mostofi, J. R. Yates, Y.-S. Lee, I. Souza, D. Vanderbilt, and N. Marzari, Comput. Phys. Commun. **178**, 685 (2008).
[32] E. Parthé, L. Gelato, B. Chabot, M. Penzo, K. Cenzual, and R. Gladyshevskii, TYPIX *Standardized Data and Crystal Chemical Characterization of Inorganic Structure Types* (Springer, Berlin/Heidelberg, 1993).
[33] O. V. Lounasmaa, Phys. Rev. **133**, A219 (1964).
[34] P. W. Selwood, *Magnetochemistry* (Interscience, New York, 1956), p. 78.
[35] J. Laverock, T. D. Haynes, C. Utfeld, and S. B. Dugdale, Phys. Rev. B **80**, 125111 (2009).
[36] M. D. Johannes and I. I. Mazin, Phys. Rev. B **77**, 165135 (2008).
[37] L. P. Gor'kov, Phys. Rev. B **85**, 165142 (2012).